Consequence of doping mediated strain and the activation energy on the structural and optical properties of ZnO:Cr nanoparticles

Richa Bhargava [a], Prashant K. Sharma [b], Sanjeev Kumar [c], Avinash C. Pandey [b], Naresh Kumar [a,*]

[a] Department of Physics, Motilal Nehru National Institute of Technology, Allahabad 211004, India
[b] Nanophosphor Application Center, University of Allahabad, Allahabad 211002, India
[c] Shah-Schulman Centre for Surface Science and Nanotechnology, Dharmsinh Desai University, Nadiad 387001, India

ABSTRACT

We report on the sol–gel synthesis of $Zn_{1-x}Cr_xO$ ($x=0.0$, 0.05, 0.10, 0.15 and 0.20) nanoparticles. These nanoparticles were characterized by using thermogravimetry/differential scanning calorimetry (TG/DSC), X-ray diffraction (XRD), transmission electron microscopy (TEM), Raman and Photoluminescence (PL). Electronegativity of Cr ions (Cr^{3+}) reduces the final decomposition temperature by 40 °C and activation energy of the reaction when Cr is doped into ZnO. Doping of higher Cr concentration ($x \geq 0.10$) into ZnO shows formation of secondary spinel ($ZnCr_2O_4$) phase along with the hexagonal (ZnO) and is revealed by XRD. Formation of secondary phase changes the activation energy of the reaction and thus the strain in ZnO lattice. In Raman spectra, additional Raman modes have been observed for $Zn_{1-x}Cr_xO$ nanoparticles, which can be assigned to the modes generated due to Cr doping. The Cr doping into ZnO is also supported by PL, in which vacancies are formed with Cr ion incorporation and emission band shifts towards higher wavelength.

© 2010 Elsevier Inc. All rights reserved.

1. Introduction

Over the past few years, II–VI semiconductors have been intensively studied for photonics and optoelectronic applications [1–3]. Among II–VI semiconductors, ZnO-based semiconductors have evoked tremendous interest due to their wide band gap of 3.32 eV and large exciton binding energy of 60 MeV for various applications such as, spintronics, photonics, optoelectronics, light emitting diodes (LEDs), solar cells, laser diodes, cosmetics, antibiotic material and gas sensors [4–8]. Transition metal (TM) doping into ZnO, have also attracted researchers for the possible multifunctional device applications. Different TMs such as Cu, Fe, Co, Mn, Ti, Cr, etc. induces magnetism when doped into ZnO and used as dilute magnetic semiconductors (DMS). Doping of TM into ZnO also alters optical properties of ZnO [6]. Magnetic properties of DMS (TM-doped ZnO) have been paid more attention than their thermal and optical properties. Another issue of secondary phase formation in transition metal doped ZnO and their effects on the thermal, optical, structural, transport and magnetic properties of ZnO is also of significant scientific concern.

Thota et al. [8] recently studied the sol–gel synthesis of ZnO powders containing Ni, Co and Mn. They have reported the solubility limit of TM into ZnO structure i.e. the concentration after which secondary phase formation takes place. The thermal,

structural and magnetic properties of TM-doped ZnO powders depend on the kind of TM and their concentrations. There are few reports on tuning of the band gap after doping of TM into ZnO [9]. Sharma et al. [10,11] observed change in magnetic behavior of ZnO with doping concentration of Cu and Fe. Singh et al. [6], on the other hand, explained the optical and magnetic properties of TM (Fe, Ni, Cu) doped ZnO based on defects and impurity states of the TM ions in ZnO lattice. Srivastava et al. [12] mentioned that the doping of Fe and secondary phase of $ZnFe_2O_4$ could quench the visible emission, whereas, large room temperature magnetization has been reported in case of nanocrystalline $ZnFe_2O_4$ thin films [13]. Palomino et al. [14] studied Fe-doped ZnO nanocrystals. The ferromagnetism in single phase Fe-doped ZnO at room temperature was observed by them. We have also recently reported the changes induced by Co concentration on structural, thermal and optical properties of ZnO [15]. In this study Co shows solubility up to 15 wt% in ZnO. Whereas, Ghosh et al. [16] studied the change in dielectric constant of ZnO nanoparticles with Co and observed that dielectric constant decreases with Co introduction. Varghese et al. [17] also observed that doped ZnO exhibit different spectroscopic properties from the pure ZnO.

Studies have also been carried out on Cr-doped ZnO nanoparticles and thin films. Wang et al. [18] studied soft chemistry route prepared Cr-doped ZnO and effect of Cr doping on magnetic property of ZnO. On the other hand, Zhuge et al. [19] studied the room temperature ferromagnetism in Cr-doped ZnO thin films. Both have reported that Cr-doped ZnO nanoparticles as well as thin films exhibit room temperature ferromagnetism but origin of

the ferromagnetism is still unclear. The optical and micro structural changes induced by Cr into ZnO have been studied by Singh et al. [6]. They have reported that Cr doping into ZnO can change the recombination wavelength and shifts towards higher wavelength. Another interesting application related to Cr-doped ZnO is that it can be used for sensing humidity as $ZnCr_2O_4$–ZnO composites can be used as a humidity sensor [20].

In the present study, we have systematically studied the effect of Cr concentration on thermal decomposition of precursors, structural, micro structural and optical properties of ZnO. We have also investigated the effect of secondary phase formation on different properties of ZnO nanoparticles.

2. Experimental details

For synthesizing Cr-doped ZnO nanoparticles, $Zn_{1-x}Cr_xO$ ($x=0.0$, 0.05, 0.10, 0.15 and 0.20), sol–gel method was used. Zinc nitrate hexahydrate ($Zn(NO_3)_2 \cdot 6H_2O$), chromium nitrate hexahydrate ($Cr(NO_3)_3 \cdot 6H_2O$), and oxalic acid ($C_2H_2O_4$) were used as starting chemicals without any further purification. Here, oxalic acid works as a chelating agent. All these chemical ingredients were weighed in stoichiometric proportions and dissolved in 100 ml of double distilled water. One of these sets, remained undoped, whereas in the remaining sets, chromium nitrate was added to obtain the sol containing $x=0.05$, 0.10, 0.15 and 0.20 in $Zn_{1-x}Cr_xO$ and continuously stirred with the help of magnetic stirrer (DBK-5058/7). Thus obtained sol was then kept in an oven (META-LAB) at 100 °C for 8 h. It was again stirred at 70 °C using a magnetic stirrer with hot plate to obtain gel. This gel was then aged for 18 h at room temperature, before the calcination. This dried gel was used as a precursor for the thermal analysis and also calcined at temperature of 700 °C in a furnace (META-LAB) for 3 h to obtain powders. The furnace was switched off and allowed to cool down up to room temperature naturally. The five sets of obtained powder were then characterized for their structural and optical properties.

For the thermal study of precursors, thermo gravimetric/differential scanning calorimeter (TG/DSC) curves were recorded. These curves of undoped and chromium doped zinc oxalate precursors were recorded using Perkin Elmer Pyris Diamond TG/DTA/DSC 8.0 series analyzer. Structural properties were investigated by Rigaku D/max-2200 PC diffractometer operated at 40 kV/20 mA, using $CuK\alpha_1$ radiation with wavelength of 1.54056 Å in the Bragg's diffraction angle '2θ' ranging from 25° to 70°. The size and morphology of the prepared particles were obtained by using a transmission electron microscope (TEM) model Technai 30 G ^{2} S-Twin electron microscope operated at 300 kV accelerating voltage. For TEM, the as-synthesized powders were dissolved in ethanol and then a drop of this dilute ethanolic solution was placed on the surface of copper grid. Raman spectra were taken with a Reinshaw micro-Raman spectroscope using 514 nm Ar+ laser as excitation source. Photoluminescence (PL) studies were performed for $\lambda_{ex}=325$ nm on a Perkin Elmer LS 55 luminescence spectrophotometer using a Xenon discharge lamp as excitation source, equivalent to 20 kW for 8 μs duration at room temperature.

3. Results and discussions

3.1. Thermo gravimetric-derivative thermo gravimetric/differential scanning calorimetry analysis (TG-DTG/DSC)

To study the thermal stability of the $Zn_{1-x}Cr_xO$ ($x=0.0$, 0.05, 0.10, 0.15 and 0.20) precursors TG-DTG/DSC curves were recorded and are shown in Fig. 1. It depicts weight loss and heat flow

occurred during different reactions carried out to obtain $Zn_{1-x}Cr_xO$ ($x=0.0$, 0.05, 0.10, 0.15 and 0.20) nanoparticles. We have used pure and mixed metal oxalate precursors for the analysis. These precursors were obtained from the gel dried in an oven at 80 °C for 1 h. Thus obtained precursors were heated in the presence of nitrogen atmosphere at the rate of 10 °C/min.

Thermal decomposition of pure zinc oxalate ($Zn_2C_2O_4 \cdot 2H_2O$) took place in three well defined steps as shown in Fig. 1(a). In this case, first stage of weight loss takes place in the temperature range 100–160 °C with endothermic peak at 155 °C. The 33.26 J/g enthalpy change occurs during this dehydration of hydrate $Zn_2C_2O_4$ precursors. Introduction of Cr nitrate into Zinc oxalate results into mixed metal oxalate. For the precursor containing smallest concentration of Cr i.e. $x=0.05$ dehydration of mixed oxalate occurs in temperature range of 102–190 °C with an endothermic peak at 161.97 °C (see Fig. 1(b)). The weight loss of 31% is recorded in this temperature range. This dehydrated mixture remains stable up to 300 °C. Above this temperature, two more steps in the temperature range 300–328 °C and 336–410 °C are observed, having a corresponding weight loss of about 2% and 29%.

The 2% and 29% weight loss may occur due to the presence of two different oxalate precursors in gel.

For higher Cr-concentration ($x \geq 0.10$) two step weight loss is observed. As seen in Fig. 1, the first step observed for pure and mixed oxalate precursors correspond to the dehydration of hydrate precursor. For mixed precursors (i.e. $x=0.05$, 0.10, 0.15, and 0.20) it is interesting to note that there exist a shoulder along with prominent endothermic peak. This may attribute to the dehydration of Cr-oxalate and Zn-oxalate precursors at two different temperatures. Similar observations were also reported by Gabal et al. [21] in case of zinc oxalate–iron oxalate mixture. The stages of these samples with weight loss, peak position and peak area are presented in Table 1.

It has also been observed that the stability of a mixture decreases from 300 to 280 °C as we increase Cr content from $x=0.05$ to $x=0.20$ in Zn-oxalate precursor. For pure zinc oxalate precursor final decomposition temperature is near 450 °C, whereas with the addition of Cr into Zn oxalate precursor it suddenly reduces to 410 °C. It is interesting to note that further increase of Cr into Zn precursor does not affect the final decomposition temperature. Mohamed et al. [22] reported that metal oxalate stability depends upon bivalent cations present in the system. Gabal et al. [21] also explained that for metal oxalate precursor's decomposition takes place for the temperatures at which the rupturing of M–O bond or C–O bond occurs. Cr ion being more electronegative than Zn ion, Cr incorporation increases the electronegativity near Zn ion strengthening Zn–O covalent bond. Hence, C–O being weak in comparison to Zn–O and Cr–O, requires less energy to break, resulting lowering in decomposition temperature. Additionally, observation of reduction in thermal stability after incorporating Cr into ZnO might be due to the decomposition of Cr oxalate at a lower temperature.

3.2. X–ray diffraction

Structural properties of $Zn_{1-x}Cr_xO$ were investigated by XRD. Fig. 2 shows the XRD of $Zn_{1-x}Cr_xO$ ($x=0.0$, 0.05, 0.10, 0.15 and 0.20). It has been observed from Fig. 2 that there are nine XRD peaks for $x=0.0$ and $x=0.05$, and all these peaks are indexed as hexagonal wurtzite structure of ZnO [23] ,however, for all other concentrations more peaks start appearing in addition to these nine peaks. One may note that as Cr-doping is increased to $x=0.10$, some additional peaks start emerging and become more prominent at higher Cr doping of $x=0.20$. These additional peaks
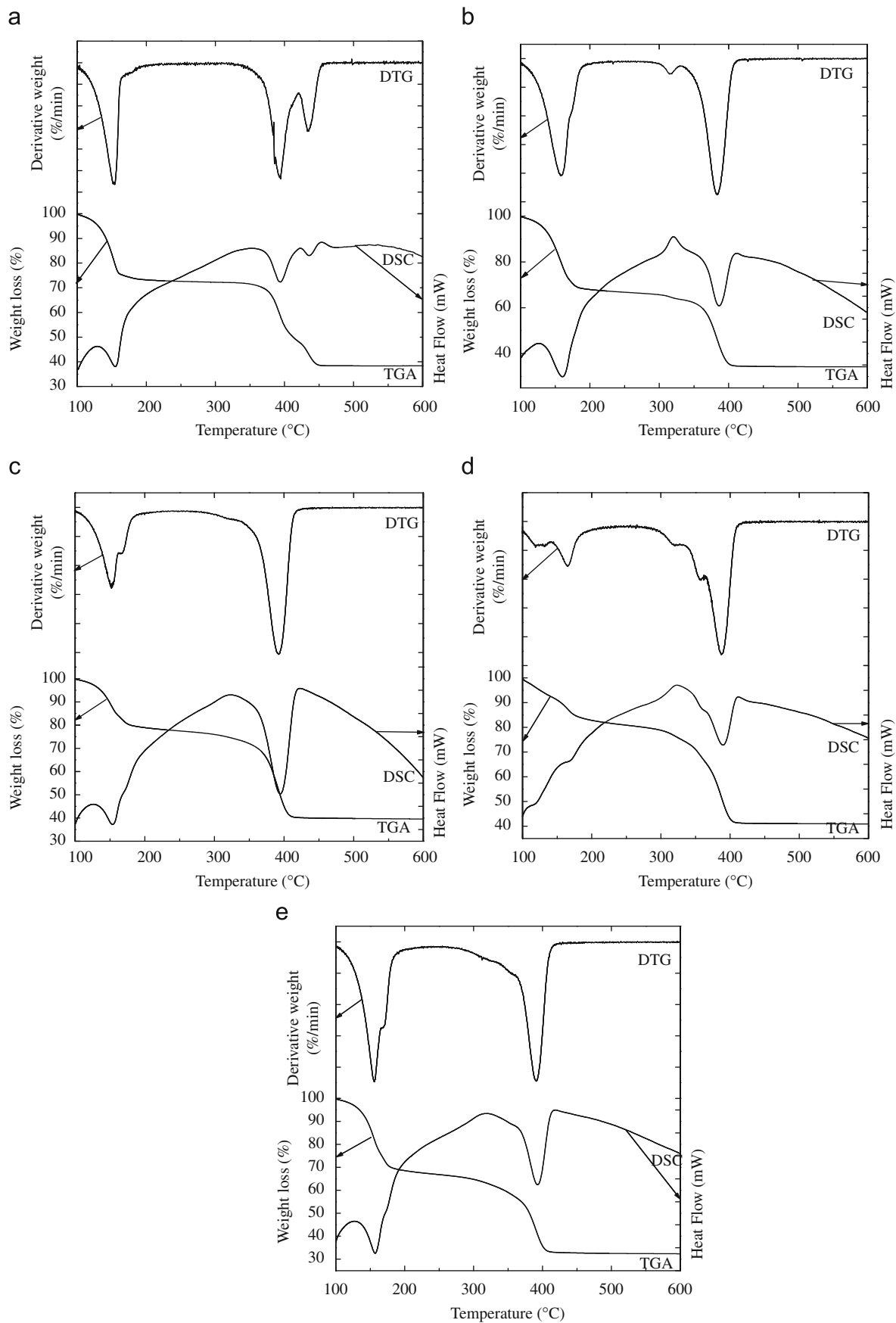
Fig. 1. TG/DTG/DSC curve of $Zn_{1-x}Cr_xO$ ((a)$x=0.0$, (b)$x=0.05$, (c)$x=0.10$,(d)$x=0.15$ and (e)$x=0.20$) precursors.

Table 1
Thermogravimetry and differential scanning calorimetry profile.

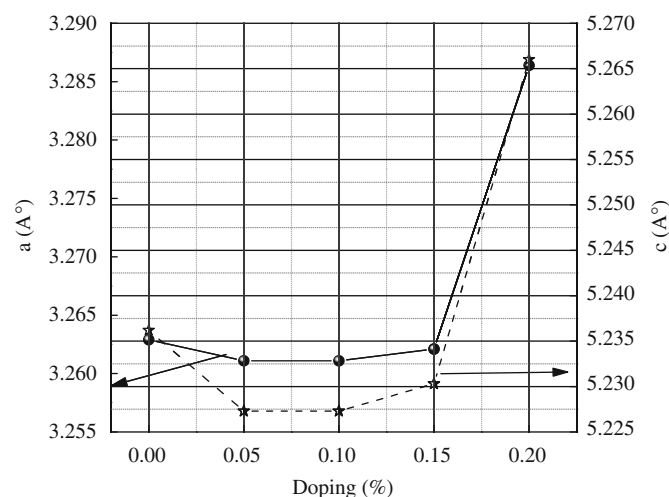| Composition	Weight loss (%)	Temperature range (deg.)	Endothermic peak (deg.)	Peak area
ZnO	24	100–159	154	108.12
	27	365–400	394	269.12
	5	400–447	436	564.87
$Zn_{1-x}Cr_xO$ ($x=0.05$)	31	100–185	161.97	957.31
	2	300–328	320.21	180.29
	29	336–410	385.79	623.23
$Zn_{1-x}Cr_xO$ ($x=0.10$)	20	100–185	154.66	237.16
	33	300–410	394.76	1556.05
$Zn_{1-x}Cr_xO$ ($x=0.15$)	16	100–190	14.38	35.41
	37	290–410	390.28	407.53
$Zn_{1-x}Cr_xO$ ($x=0.20$)	30	100–194	157.89	1010.48
	32	280–410	393.13	824.12
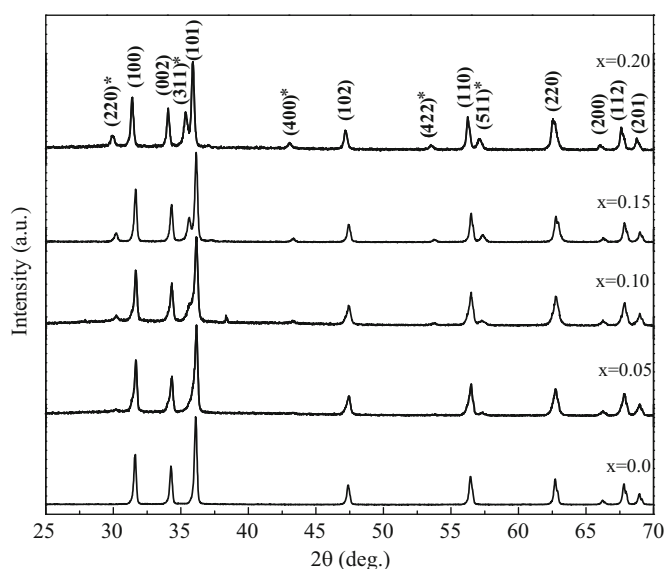
Fig. 2. XRD patterns of $Zn_{1-x}Cr_xO$ ($x=0.0$, 0.05, 0.10, 0.15 and 0.20) powders obtained after the calcination at 700 °C for 3 h. (* represents the secondary phase of $ZnCr_2O_4$.)

Fig. 3. Variation in lattice parameters (a and c) with Cr doping concentration.

were indexed to (2 2 0), (3 1 1), (4 0 0), (4 2 2) and (5 1 1) of spinel $ZnCr_2O_4$. The lattice parameters 'a' and 'c' for ZnO phase were calculated for $Zn_{1-x}Cr_xO$ ($x=0.0$, 0.05, 0.10, and 0.20).

The values of lattice parameters as a function of Cr-doping are shown in Fig. 3. It is interesting to note that the values of 'a' and 'c' first decrease as Cr is increased up to $x=0.10$ then increases for higher Cr doping ($x \geq 0.15$). The first decrease in lattice parameters are quite obvious as Cr ions (Cr^{3+}) are of smaller ionic radii then Zn ions (Zn^{2+}). A similar decrease in 'a' and 'c' was observed in case of Cr-doped ZnO nanoparticles by Liu et al. [24]. According to Vegard's law [25] change in lattice parameter with doping percentage should vary linearly, however, it is not the case in present study. The deviation from the linearity or from Vegard's law can be attributed to the interstitial incorporation of Cr in $Zn_{1-x}Cr_xO$ and to the fact that at higher concentration Cr is not soluble into ZnO. As observed from the XRD data, the solubility limit of Cr into ZnO is up to $x=0.05$ as above this concentration secondary spinel phase of $ZnCr_2O_4$ can be seen. Recently, deviation in the Vegard's law has also been reported in case of $Zn_{1-x}Mg_xO$ thin films by Reddy et al [25]. The change in lattice parameter with Cr concentration may also be due to the formation of defects. Different reaction can give rise to different defect volume leading to the change in lattice parameters. The sudden increase in lattice parameters for the highest Cr concentration i.e. $x=0.20$, may be because of phase transformation from hexagonal ZnO towards the cubic spinel

$ZnCr_2O_4$. The lattice parameter 'a' for the additional spinel phase was also calculated for $x=0.10$, 0.15 and 0.20 and were found to be 8.3522, 8.3453 and 8.4056 Å respectively, those were close to the bulk (JCPDS no. 731962) [26]. The average crystallite sizes (D) for $Zn_{1-x}Cr_xO$ have been estimated by using the Scherrer's formula [27]. The lattice strain and effective crystallite size were also calculated by implying the Williamson and Hall equation [27].

The curve $\beta \cos\theta/\lambda$ is plotted against $\sin\theta/\lambda$ for $Zn_{1-x}Cr_xO$ and is shown in Fig. 4(a)–(e). The effective lattice strain and crystallite size were estimated from the slope and intercept of linear fitting of the curve, respectively. The calculated values of D, ε, η for different Cr doping into ZnO is tabulated in Table 2. It can be seen from the table, the crystallite size first decreases for $x=0.05$ then increases for $x=0.15$ and again drops down for the highest Cr doping of $x=0.20$. It is very much surprising to note that the lattice strain (η) follows an exactly opposite trend than the crystallite size. Since, XRD data of our samples clearly reveals co-existence of spinel ($ZnCr_2O_4$) and hexagonal (ZnO) phases in Cr-doped ZnO ($x \geq 0.10$) nanoparticles. There might be two possible reasons causing strain in a system where two-phases co-exist. It may be either due to lattice misfit at the interface between these two phases or due to the deformation arising from volume differences between the two phases [28]. Recently, Addonizio et al. [29] have observed that the strain in the thin films of boron-doped ZnO follows an opposite trend as that of crystallite size and attributed this to the impurities segregation at the grain boundaries. Increase in strain with the decrease in crystallite size has also been reported in case of α-Fe_2O_3 nanoparticles prepared by ball milled technique and the behavior was explained
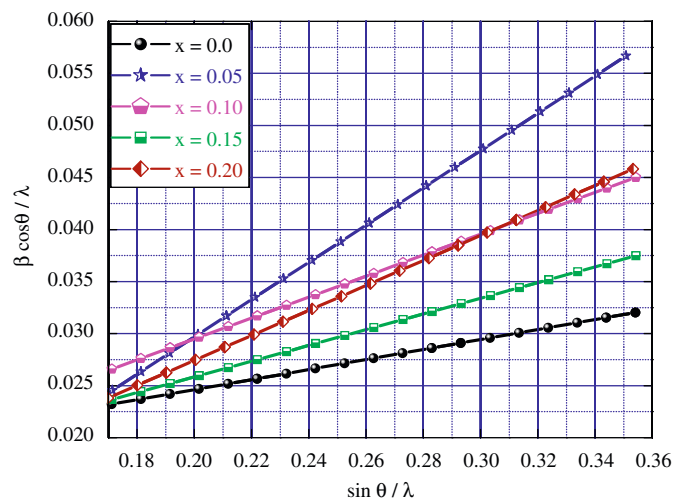
Fig. 4. Lattice strain calculation for $Zn_{1-x}Cr_xO$ ($x=0.0$, 0.05, 0.10, 0.15 and 0.20) powders.

Table 2
Parameters calculated using XRD data.

Composition	D (nm)	ε (nm)	η
ZnO ($x=0.0$)	35	43	0.0481
$Zn_{1-x}Cr_xO$ ($x=0.05$)	26	36	0.1650
$Zn_{1-x}Cr_xO$ ($x=0.10$)	27	41	0.0975
$Zn_{1-x}Cr_xO$ ($x=0.15$)	32	42	0.0655
$Zn_{1-x}Cr_xO$ ($x=0.20$)	29	41	0.1081

by the formation of defects during milling process [30]. The variation in strain and crystallite size is thus clearly governed by the concentration of Cr dopant in the host ZnO matrix. At lower Cr concentration ($x=0.05$ and 0.10), the decrease in size and increase in strain may be observed due to the replacement of Zn ions by Cr ions. Sudden change in the trend as observed at $x \geq 0.15$ may arise due to the secondary spinel phase formation.

3.3. Transmission electron microscopy (TEM)

To see the effect of Cr doping on the particle size and their shape have been studied using transmission electron microscopy. Fig. 5(a–c) shows the bright field image of for $Zn_{1-x}Cr_xO$ ($x=0.00$, 0.05 and 0.20) powders. As seen from the figure, all the particles are having a spherical shape. For the undoped ZnO the agglomeration is more, whereas with the Cr doping ($x=0.05$) agglomeration decreases. The average particle sizes of these particles were calculated using bright field TEM images. About 30–35 particles were considered to calculate an average particle size. For the undoped ZnO average particle size was 70 nm. It is interesting to note that with the Cr doping into ZnO reduces the particle size. The average particle size was ~45 nm, which further decreases with an increase in the Cr concentration and was observed to be 40 nm for $x=0.20$. The particle size distribution curve for $x=0.0$, $x=0.05$ and $x=0.20$ is shown in Fig. 5(d–f). As seen from Table 2 average and effective crystallite sizes are smaller from the particle size obtained from the TEM the reason being one particle can have one or more crystallite [15].

3.4. Kinetics studies

The kinetics of the oxalate decomposition steps (last decomposition step) of anhydrous pure and mixed oxalate

($Zn_{1-x}Cr_xC_2O_4 \cdot 2H_2O$ ($x=0.0$, 0.05, 0.10, 0.15 and 0.20)) have been studied under non-isothermal condition. The modified Coats-Redfern method was used to calculate the activation energy of the final decomposition step of all reactions from the TG curves. In modified Coats-Redfern method [21], decomposition can be expressed as

$$\frac{-\ln(1-\alpha)}{T^2} = \frac{AR}{\beta E_a} e^{E_a/(RT)} \tag{1}$$

The above equation can be re-written by taking natural logarithm and can be expressed as

$$\ln\left[\frac{-\ln(1-\alpha)}{T^2}\right] = \ln\left(\frac{AR}{\beta E_a}\right) - \frac{E_a}{RT} \tag{2}$$

where α is different fractional reaction; T is absolute temperature; A is frequency factor; R is universal gas constant; β is heating rate; and E_a is activation energy.

A plot of $\ln\left[\frac{-\ln(1-\alpha)}{T^2}\right] vs \frac{1}{T}$ was used to calculate activation energy (see Fig. 6). Thus obtained values of activation energies of all the reactions are presented in Table 3. As seen from the table, activation energy for Zn-oxalate precursor decreases for $x=0.05$. Further, with the increase in Cr content ($x=0.10$ and 0.15) activation energy increases and again decreases for the highest Cr-content. As discussed in earlier section that the introduction of Cr ions into zinc oxalate will increase electronegativity around Zn resulting increase in reactivity of Zn–O bond and thus decrease in activation energy.

The increase in activation energy may attribute to new phase formation for $x=0.10$ and 0.15. Since Cr ions may react separately to form another spinel phase of $ZnCr_2O_4$ thus decomposition may require more energy to rupture the bonds. Further decrease in E_a for $x=0.20$ may be due to the fact that for this concentration, $Zn_{1-x}Cr_xC_2O_4 \cdot 2H_2O$ has enough Cr ions. So it can easily form the spinel phase as well as supports the Zn ions to form ZnO phase requiring less energy to rupture the bonds.

A relation has been observed in between Cr concentration, activation energy, strain and crystallite size. From the above results it is clear that when we introduce Cr ions into ZnO ($x=0.05$) it may replace the Zn^{2+} ions from ZnO lattice that introduces strain in the lattice and in this case there may be only one reaction going on, that was well supported by Cr ions, which further decrease the activation energy. As we increase Cr amount in ZnO ($x=0.10$ and 0.15) the activation energy increases. This may occur due to the reason that single reaction process is now changing to two reactions process, which takes place together simultaneously. Hence, Cr ion has to participate in two reactions. Now for $x=0.10$ and 0.15, Cr ions may not be supporting the Zn ion's reaction. Thus more energy is required to rupture the bond which in turn reduces the strain in ZnO lattice. This can be verified using XRD of $x=0.10$ and 0.15, which shows signatures of secondary spinel phase of $ZnCr_2O_4$.

Interestingly, for highest Cr doping of $x=0.20$, activation energy decrease whereas, strain increases. For this concentration, both the reactions are still going on simultaneously. However, the amount of Cr is now very high and precursor is having enough Cr ions to complete both the reactions. Thus, in this case, Cr not only gives its electronegativity to Zn ion but also forms another phase.

This decrease/increase in activation energy can be attributed to the decrease/increase in crystallite size [31–33]. In the present study it has been observed that for smaller particles activation energy is less whereas as it changes when the size changes. It may be understood as particles with smaller size contain more defects in the lattice enabling reaction to occur easily. Also, lowering of particle dimensions increases surface energy resulting decrease in the activation energy of the reaction. Reduction in particle size
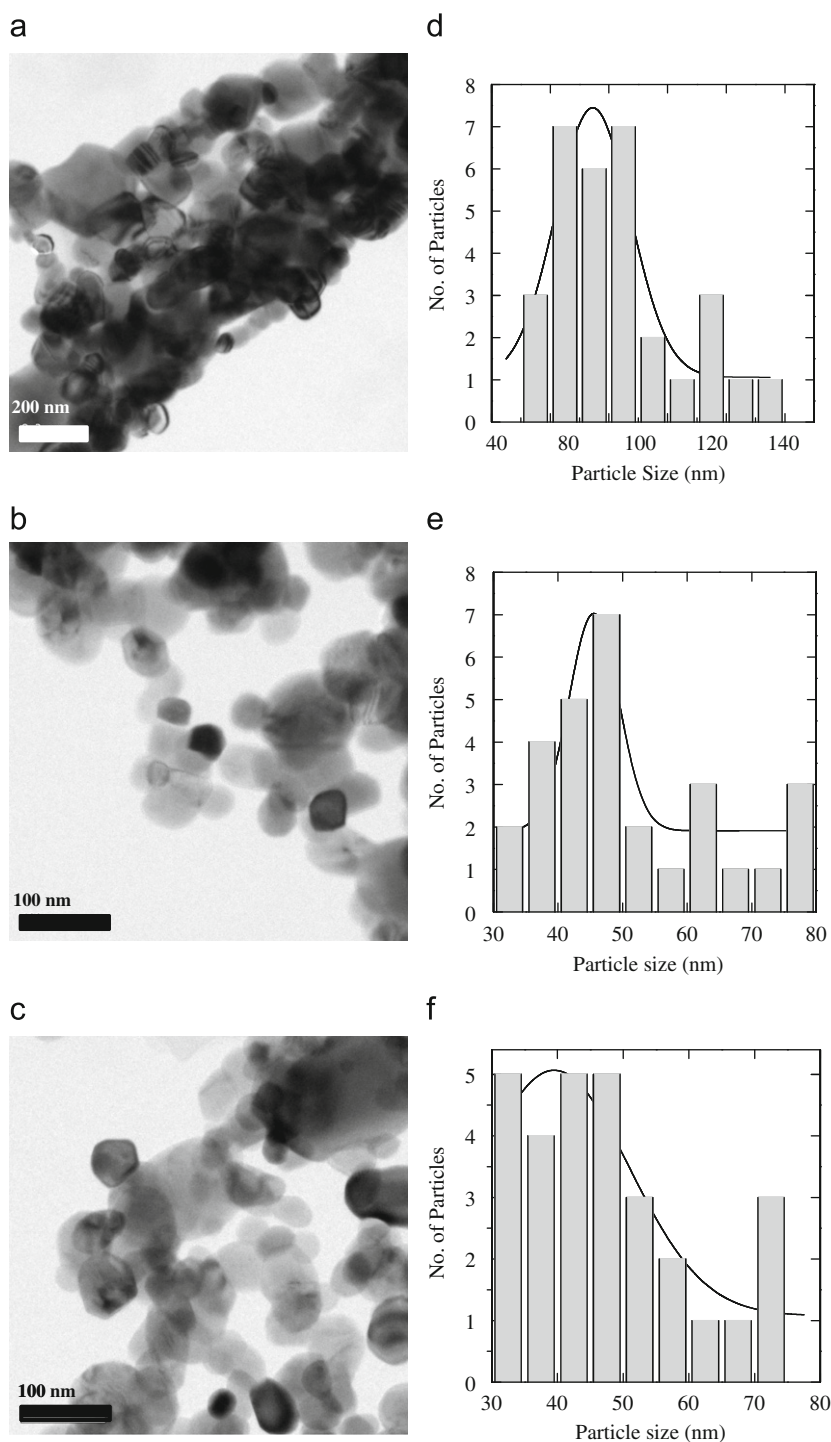
a

d

b

e

c

f

Fig. 5. (a,b,c) TEM images of $Zn_{1-x}Cr_xO$ ($x=0.0$, 0.05 and 0.20) and (d,e,f) Particle size distribution of ($x=0.0$, 0.05 and 0.20) nanoparticles.

along with aggregation causes intergrain defects, and affects the activation energy of the reaction. The activation energy thus may be one of the parameter controlling strains and crystallite size for $Zn_{1-x}Cr_xO$ nanoparticles.

3.5. Raman spectroscopy

To see the effect of Cr doping on ZnO symmetry and vibrational modes, Raman spectra for Cr-doped ZnO have been recorded. Fig. 7 shows the Raman spectrum of undoped and Cr-doped ZnO.

ZnO is reported to have hexagonal wurtzite structure, which belongs to C_{6v}^4 space group with two formula units per primitive cell [15]. According to the group theory there exist eight sets of the zone center optical phonons and can be represented as $\Gamma_{opt}=A_1+E_1+2E_2$. The Raman active phonons of A_1 and E_1 symmetry are polar phonons, whereas phonons of E_2 symmetry are non-polar. Polar modes can be split into transverse (TO) and longitudinal (LO) optical phonons exhibiting different wavenumbers. In case of non-polar Raman active phonon modes, E_2 can have two wavenumbers: E_2 (low) and E_2 (high).
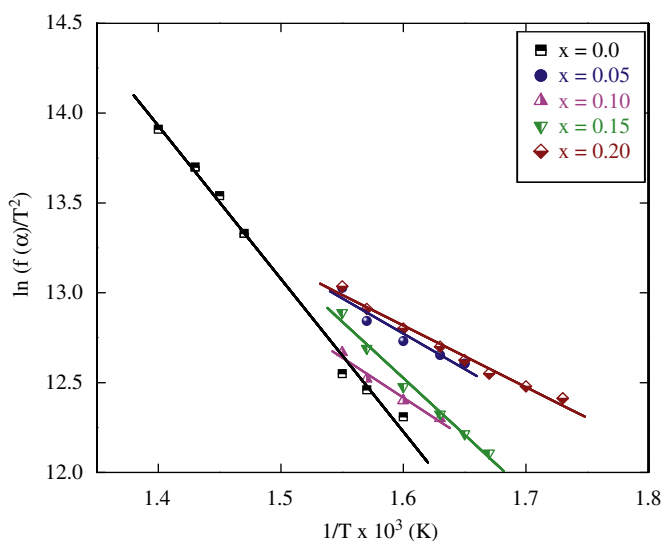
Fig. 6. Plot to calculate activation energy of $Zn_{1-x}Cr_xO$ ($x=0.0$, 0.05, 0.10, 0.15 and 0.20) systems.

Table 3
Thermodynamics parameters of $Zn_{1-x}Cr_xO$ ($x=0.0$, 0.05, 0.10, 0.15, 0.20)system.

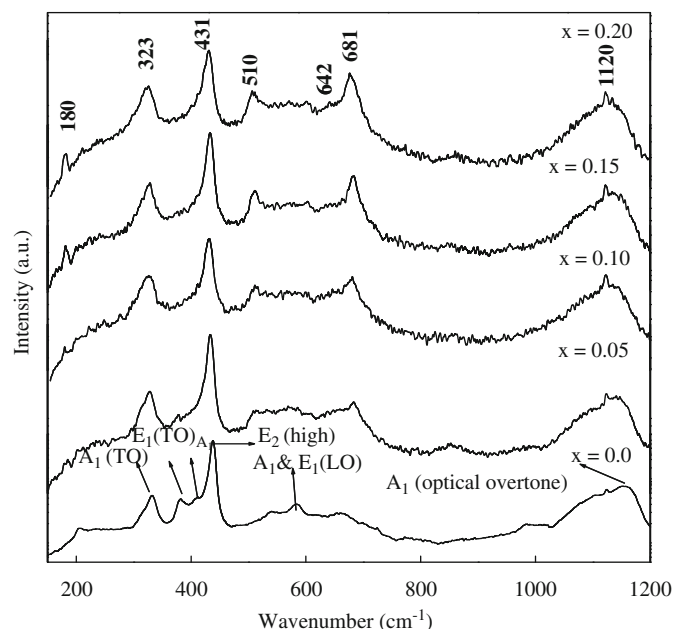| Composition	ΔH (KJ/mol)	ΔS (KJ/Kmol)	ΔG (KJ)	E_a (KJ/mol)
$x=0.0$	31.56	10.71	−4672.59	168.00
$x=0.05$	11.14	7.74	−2977.46	75.42
$x=0.10$	22.22	17.02	−6698.72	151.17
$x=0.15$	8.89	25.21	−9833.46	163.86
$x=0.20$	13.85	21.78	−8552.19	70.05

Fig. 7. Raman spectrum of $Zn_{1-x}Cr_xO$ ($x=0.0$, 0.05, 0.10, 0.15 and 0.20) systems.

From Fig. 7, it has been observed that for undoped ZnO nanoparticles all active modes near 332, 380, 410, 437, 537, 580, 658 and $1150\,cm^{-1}$ appear in Raman spectra correspond to ZnO. The Raman active modes near 380, 410, 437 and $580\,cm^{-1}$ represents the first order phonon spectrum, whereas, other peaks

at 332, 537 and 658 represents the second order phonon spectrum [34]. Raman mode near $380\,cm^{-1}$ corresponds to transverse optical phonon for A_1 symmetry i.e. A_1 (TO). For E_1 symmetry, E_1 (TO) mode appears near $410\,cm^{-1}$. The peak near $437\,cm^{-1}$ is due to the typical Raman active in wurtzite structure and corresponds to E_2 (high) Raman mode for ZnO, whereas, the peak at $580\,cm^{-1}$ is positioned between A_1 (LO) and E_1 (LO). A broad peak situated at $1150\,cm^{-1}$ may correspond to optical overtone. As observed from Fig. 7, for $Zn_{1-x}Cr_xO$ ($x=0.05$, 0.10, 0.15 and 0.20), some of the Raman active modes associated with ZnO disappears whereas, new peaks starts appearing as we introduce Cr into ZnO lattice. With the small amount of Cr into ZnO ($x=0.05$), peak due to the transverse optical modes of A_1 and E_1 symmetry i.e. A_1 (TO) and E_1 (TO) diminishes and finally disappear for the higher concentration of Cr i.e. $x \geq 0.15$. Moreover, additional peaks near 510 and $680\,cm^{-1}$ appear with Cr doping into ZnO gets intensified for the higher Cr concentration i.e. ($x=0.15$ and 0.20).

From the XRD data, it has already been revealed that for $x=0.15$ and 0.20 there is a co-existence of $ZnCr_2O_4$ and ZnO phase. $ZnCr_2O_4$ has a cubic spinel structure with a space group of $Fd3m$. There are five Raman active modes (one A_{1g}, one E_g, and three F_{2g}) of the spinel phase as suggested by group theory [35]. For the smallest doping of Cr into ZnO i.e. $x=0.05$, the Raman peaks near 380, 410, 537 and $580\,cm^{-1}$, disappear and two peaks near 510 and $680\,cm^{-1}$ starts emerging. As Cr concentration into ZnO is increased ($x \geq 0.10$) peaks near 510 and 680 become prominent. For $x \geq 0.15$, one can easily see five peaks in the Raman spectra. Peaks near 180, 510 and $600\,cm^{-1}$ correspond to F_{2g} mode of spinel $ZnCr_2O_4$. The peak near $680\,cm^{-1}$ is due to A_g symmetry of spinel phase. It should be noted that the peak position of $320\,cm^{-1}$ peak remains unchanged even after substitution of Cr into ZnO. It is further interesting to note that the peak observed at $437\,cm^{-1}$ for undoped ZnO (representing wurtzite hexagonal structure of ZnO) starts broadening and shifting as Cr is doped into ZnO, finally the peak is moved to $431\,cm^{-1}$. This shifting of the peak from 437 to $431\,cm^{-1}$ clearly indicates the structural distortion from wurtzite of ZnO to spinel $ZnCr_2O_4$. However, the unchanged peak near $329\,cm^{-1}$ confirms the existence of ZnO phase along with $ZnCr_2O_4$.

The Raman modes of $ZnCr_2O_4$ have been studied by different groups. Stanojevic et al. [36] have shown the Raman active modes of $ZnCr_2O_4$ spinel in the spectral range of $150–900\,cm^{-1}$ and observed group of strong bands between 500 and $700\,cm^{-1}$ and low wave number band with a weak intensity below $250\,cm^{-1}$. All the peaks were assigned to the Raman active modes of $ZnCr_2O_4$. Wang et al. [35] also observed five Raman active modes of spinel $ZnCr_2O_4$. However, broadening of Raman peaks ($\sim$430 cm^{-1}) with the increase in Cr have been reported and attributed to the cation–anion bond length and polyhedral distortion occurring in $ZnCr_2O_4$. Hauike et al. [37] reported the broadening of Raman peaks with the Co doping and explained this to the alloying effect, which takes place due to compositional fluctuations caused by random substitution of Co into ZnO. Recently, we have reported similar broadening in the Raman peaks after doping Co into ZnO [15]. In addition to this, broadening of peak near $430\,cm^{-1}$ may also arise due to combined effect of two Raman modes i.e. $430\,cm^{-1}$ of $ZnCr_2O_4$ and $437\,cm^{-1}$ of ZnO. Detailed Raman active modes along with their symmetry as observed with the variation in Cr doping are presented in Table 4.

3.6. Photoluminescence

To study the influence of Cr doping on emission and defects formations, photoluminescence spectra of $Zn_{1-x}Cr_xO$ ($x=0.0$,

Table 4
Raman vibration modes (cm^{-1}) along with the assigned symmetry.

Symmetry	$Zn_{1-x}Cr_xO$			
	$x=0.05$	$x=0.10$	$x=0.15$	$x=0.20$
F_{2g}[a]			180	180
A_1(acoustic overtone)	324	323	323	323
$E_{1(TO)}$	380			
E_{2H}/E_g[a]	434	432	431	431
F_{2g}[a]	506	508	510	521
A_g[a]	680	680	681	681
Optical overtone	1138	1130	1123	1125

[a] Represent the vibration modes $ZnCr_2O_4$.
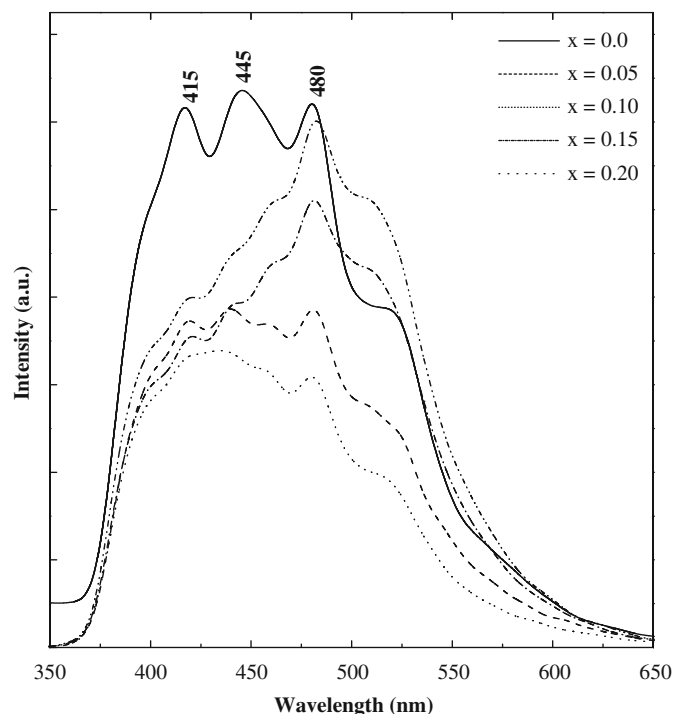
Fig. 8. PL spectrum of $Zn_{1-x}Cr_xO$ ($x=0.0$, 0.05, 0.10, 0.15 and 0.20) systems.

0.05, 0.10, 0.15 and 0.20) were recorded and presented in Fig. 8. For undoped ZnO nanopowders three prominent peaks at 415, 445 and 480 nm along with a shoulder near 520 nm. The peak near 415 nm arises due to violet emission, whereas other two peaks belong to blue emission. For the ZnO nanoparticles, majority donors for luminescence in visible regions are oxygen vacancies (V_O) and interstitial Zn (Zn_i), although other defects also control the luminescence of ZnO nanoparticles. Peaks in the visible region may be associated with the deep level emissions and can be attributed to structural defects such as interstitial (Zn_i and O_i), vacancies (V_O and V_{Zn}), and surface traps [38].

As we introduce Cr ions into the ZnO, the overall PL intensity decreases along with the peak at 415 nm. For the low Cr concentration, at $x=0.05$, peak intensity of all the peaks diminishes and peaks at 415 and 445 nm merge together to give a broad hump in that region. As we further increase Cr concentration into ZnO matrix, these two peaks start disappearing. Whereas the peak at 480 nm alone remains at the higher concentrations of Cr at $x=0.20$. A slight red shift in this peak with an increase in intensity has been observed for $x=0.20$. Thus with the increase in Cr concentration violet emission decreases.

Singh et al. [6] reported that Cr doping into ZnO suppress the recombination radiation. In the present case also it has been observed that with the Cr doping violet emission mainly caused by the recombination radiation got suppressed and can be attributed to the fact that with Cr doping non-radiative recombination process also increases. According to Behera et al. [39] the band near 480 nm arises due to the transition between the shallow donor (Zn_i) and deep acceptor (V_{Zn}). Whereas, Srivastava et al. [12] also reported intrinsic defects, particularly interstitial Zn (Zn_i) is responsible for the blue emission. Non-stoichiometric ZnO causes the formation of Zn_i. In present case as we dope ZnO, some Cr ions may replace the Zn ions from its site which in turn produces the interstitial Zn. With Cr concentration amount of non-stoichiometric ZnO increases as another phase has been observed at the high concentrations $x=0.15$ and 0.20. In addition, the increase in interstitial Zn increases the transition around 480 nm. Additional phase of spinel $ZnCr_2O_4$ exhibits a broad blue luminescence in the visible region of 300–450 nm as reported by Peng et al. [40]. Thus, increase in the transition near 480 with the increase in Cr concentration can also be occurring due to secondary phase of $ZnCr_2O_4$.

4. Conclusion

Undoped and Cr-doped ZnO, $Zn_{1-x}Cr_xO$ ($x=0.00$, 0.05, 0.10, 0.15 and 0.20) powders were successfully synthesized by thermal decomposition of oxalate precursor via sol–gel method. It has been observed that thermal decomposition temperature varies for undoped and doped oxalate precursors, and it suddenly drops by nearly 40 °C when Cr was added into it. For $x > 0.10$, an additional phase of cubic spinel $ZnCr_2O_4$ has been observed. With the Cr doping, crystallite size, lattice parameters and strain of ZnO lattice changes. This was further verified using Raman spectroscopy, which clearly shows that vibrational modes of hexagonal wurtzite structure of ZnO changes to the vibrational modes of cubic spinel phase of $ZnCr_2O_4$. Further it has been observed that Cr doping affects the luminescence emission of the ZnO. Random substitution into ZnO matrix causes the formation of interstitial Zn which further induces the non-radiative recombination. Formation of secondary phase increases the non-stoichiometric ZnO in material, which is again responsible for the emission around 480 nm.

References

[1] L. Liao, D.H. Liu, J.C. Li, C. Liu, Q. Fu, M.S. Ye, Appl. Surf. Sci. 240 (2005) 175.
[2] M. Ristic, S. Music, M. Invanda, S. Popovic, J. Alloys Compd. 397 (2005) L1.
[3] H.K. Yadav, K. Sreenivas, V. Gupta, J.F. Scott, R.S. Katiyar, Appl. Phys. Lett. 92 (2008) 122908.
[4] G. Glaspell, P. Dutta, A. Manivannan, J. Cluster Sci. 16 (2005) 523.
[5] C.J. Cong, J.H. Hong, K.L. Zhanga, Mater. Chem. Phys. 113 (2009) 435.
[6] S. Singh, E.S. Kumar, M.S.R. Rao, Scr. Mater. 58 (2008) 866.
[7] S. Oharaa, T. Mousavanda, M. Umetsua, S. Takamia, T. Adschiri, Y. Kurokib, M. Takatab, Solid State Ionics 172 (2004) 261.
[8] S. Thota, T. Dutta, J. Kumar, J. Phys.: Condens. Matter 18 (2006) 2473.
[9] S. Senthilkumaar, K. Rajendran, S. Banerjee, T.K. Chini, V. Sengodan, Mater. Sci. Semicond. Proc. 11 (2008) 6.
[10] P.K. Sharma, R.K. Dutta, A.C. Pandey, S. Layek, H.C. Verma, J. Magn. Magn. Mater. 321 (2009) 2587.
[11] P.K. Sharma, R.K. Dutta, A.C. Pandey, J. Magn. Magn. Mater. 321 (2009) 3457.
[12] A.K. Srivastava, M. Deepa, N. Bahadur, M.S. Goyat, Mater. Chem. Phys. 114 (2009) 194.
[13] M. Bohra, S. Prasad, N. Kumar, D.S. Misra, S.C. Sahoo, N. Venkataramani, R. Krishnan, Appl. Phys. Lett. 88 (2006) 262506.
[14] A. Parra-Palomino, O. Perales–Perez, R. Singhal, M. Tomar, J. Hwang, P.M. Voyles, J. Appl. Phys. 103 (2008) 07D121.
[15] R. Bhargava, P.K. Sharma, R.K. Dutta, A.C. Pandey, S. Kumar, N. Kumar, Mater. Chem. Phys. 120 (2010) 393.
[16] C.K. Ghosh, K.K. Chattopadhyay, M.K. Mitra, J. Appl. Phys. 101 (2007) 124911.
[17] N. Varghese, L.S. Panchakarla, M. Hanapi, A. Govindraj, C.N.R. Rao, Mater. Res. Bull. 42 (2007) 2117.

[18] B. Wang, J. Iqbal, X. Shan, G. Huang, H. Fu, R. Yu, D. Yu, Mater. Chem. Phys. 113 (2009) 103.
[19] L.J. Zhuge, X.M. Wu, Z.F. Wu, X.M. Chen, Y.D. Meng, Scr. Mater. 60 (2009) 214.
[20] S. Pokhrel, B. Jeyaraj, K.S. Nagaraja, Mater. Lett. 57 (2003) 3543.
[21] M.A. Gabal, A.A. El-Bellihi, H.H. Bahnasawy, Mater. Chem. Phys. 81 (2003) 174.
[22] M.A. Mohamed, A.K. Galwey, S.A. Halawy, Thermochim. Acta 429 (2005) 57.
[23] Joint Committee on Powder Diffraction Standards (JCPDS), powder diffraction file no 80-0510.
[24] Y. Liu, J. Yang, Q. Guan, L. Yang, Y. Zhang, Y. Wang, B. Feng, J. Cao, X. Liu, Y. Yang, M. Wei, J. Alloys Compd. 486 (2009) 835.
[25] A.S. Reddy, P. Prathap, Y.P.V. Subbaiah, K.T.R. Reddy, J. Yi, Thin Solid Films 516 (2008) 7084.
[26] Joint Committee on Powder Diffraction Standards (JCPDS), powder diffraction file no 73-1962.
[27] S.C. Navale, V. Ravi, I.S. Mulla, Sens. Actuators B 139 (2009) 466.
[28] T.S. Han, P.R. Dawson, Mater. Sci. Eng. A 405 (2005) 18.
[29] M.L. Addonizio, C. Diletto, Sol. Energy Mater. Sol. Cells 92 (2008) 1488.
[30] O.M. Lemine, Superlattices Microstruct. 45 (2009) 576.
[31] L.P. Ravaro, D.I. Santos, L.V.A. Scalvi, J. Phys. Chem. Solids 70 (2009) 1312.
[32] L.S. Taylor, P. York, Int. J. Pharm. 167 (1998) 215.
[33] P.L. Chang, Y.C. Wu, S.J. Lai, F.S. Yen, J. Eur. Ceram. Soc. 29 (2009) 3341.
[34] R.Y. Sato-Berrú, A. Vázquez-Olmos, A.L. Fernández-Osorio, S. Sotres-Martínez, J. Raman Spectrosc. 38 (2007) 1073.
[35] Z. Wang, P. Lazor, S.K. Saxena, G. Artioli, J. Solid State Chem. 165 (2002) 165.
[36] Z.V.M. Stanojević, N. Romčević, B. Stojanović, J. Eur. Ceram. Soc. 27 (2007) 903.
[37] N. Hauike, K. Nishio, H. Katoh, A. Suzuki, T. Isshiki, K. Kisoda, H. Harima, J. Phys.: Condens. Matter 21 (2009) 064215.
[38] P.K. Sharma, A.C. Pandey, G. Zolnierkiewicz, N. Guskos, C. Rudowicz, J. Appl. Phys. 106 (2009) 094314.
[39] D. Behera, B.S. Acharya, J. Lumin. 128 (2008) 1577.
[40] C. Peng, L. Gao, J. Am. Ceram. Soc. 91 (2008) 2388.